Surfaces and Interfaces 70 (2025) 106866

Contents lists available at ScienceDirect

Surfaces and Interfaces

journal homepage: www.sciencedirect.com/journal/surfaces-and-interfaces

A well-constructed Bi_3O_4Br/PANI composite: elevation of visible-light photocatalytic degradation performance through the synergistic mechanism of oxygen vacancies and heterojunctions

Qiao Wang [a,1], Yiwen Peng [a,1], Aobo He [a], Zhenshen Li [a], Jialin Jia [b,*], Huahong Xu [a], Yuemi Yu [a], Zhiqiang Zhang [c]

[a] School of Civil and Transportation Engineering, Guangdong University of Technology, Guangzhou 510006, China
[b] School of Environmental and Chemical Engineering, Jiangsu University of Science and Technology, Zhenjiang 212100, PR China
[c] School of Environmental and Municipal Engineering, Xi'an University of Architecture and Technology, Xi'an 710055, China

ARTICLE INFO

Keywords:
Visible-light photocatalysis
Bismuth oxyhalide
Organophosphorus
Heterojunction
Oxygen vacancy

ABSTRACT

The concerted action between oxygen vacancies and the heterogeneous interface effect is conducive to form internal electric field, which furnishes a rapid pathway for charge transfer. Here, by incorporating oxygen vacancies into bismuth-based semiconductors, the Bi_3O_4Br/PANI heterojunction structures with rich oxygen vacancies are fabricated via a simple hydrothermal method. The as-prepared optimal BBP-0.05 % nanosheets exhibit a ultrafast removal of 95 % chloroquine phosphate (CQP) within visible light irradiation for 2 min. Moreover, the corresponding apparent rate constant (k) is as high as 1.15 min^{-1}, which is 4.8 times that of Bi_3O_4Br (0.242 min^{-1}) and 25 times that of BBP-noOV (0.01754 min^{-1}), respectively. The coupling structure of oxygen vacancies and heterojunction in the Bi_3O_4Br/PANI composite is capable of significantly augmenting the visible light absorption capacity and expediting the separation and migration efficiency of photogenerated hole/electron pairs, thereby remarkably enhancing the photocatalytic performance. Through radical trapping experiments and EPR spectra, it is determined that holes and singlet oxygens play crucial roles, while superoxide radicals and hydroxyl radicals contribute secondarily, facilitating the superior catalytic performance of the Bi_3O_4Br/PANI/Vis system.

1. Introduction

During the COVID-19 pandemic, CQP has become the center of attention as a crucial and effective clinical remission drug [1]. Nevertheless, its usage is increasing on a large scale, CQP has become one of the emerging pollutants (EC). In virtue of its persistence and biotoxicity, it may pose a huge potential threat to the aquatic environment [2,3]. Visible-light photocatalytic technology represents a promising approach for degrading organophosphorus pollutants, utilizing a unique catalytic mechanism to efficiently decompose pollutants without generating secondary pollution [4–7]. However, the narrow solar light response range and low quantum efficiency are the bottlenecks in the practical application of photocatalysis [8,9], and thus it is urgent to explore more efficient strategies for designing photocatalysts with high visible-light absorption and electron separation rate [10–13]. Bi_3O_4Br is served as a semiconductor material with a moderately sized bandgap at ~2.7 eV, which can effectively absorb visible light [14]. Meanwhile, its layered structure is conducive to the separation and migration of photogenerated charges. Notably, the non-stoichiometric properties of Bi_3O_4Br offers a far lower photo-induced electron and hole recombination rate compared to the original BiOBr. However, the photocatalytic performance of intrinsic Bi_3O_4Br is still restricted by the charge separation performance.

In recent years, researchers have developed a variety of strategies to overcome the obstacle of rapid carrier recombination, such as controlling the morphology [15,16], defect engineering [17], doping [18,19], and constructing heterojunctions [20], and so on. Among them, the heterojunction has been widely favored by researchers due to its advantages such as expanding the light response range, facilitating carrier separation, and enhancing the redox ability [9,21]. Liu group [9]

* Corresponding author.
E-mail address: hit_jjl2023@126.com (J. Jia).
[1] Q Wang and Y Peng contributed to this work equally.

https://doi.org/10.1016/j.surfin.2025.106866
Received 4 February 2025; Received in revised form 31 May 2025; Accepted 3 June 2025
Available online 3 June 2025

prepared the $CsPbBr_3$ QD/$CuCo_2O_4$ NS p/n heterojunction and achieved 3.2 times and 9.2 times higher photocatalytic CO_2 to CH_4 than $CsPbBr_3$ QD and $CuCo_2O_4$ NS, respectively. Moreover, the heterojunction interface can establish a built-in electric field (IEF), which can accelerate the transfer of charge carriers without extra input energy. Meanwhile, as another highly efficient modification strategy, oxygen vacancies can not only form defect energy levels to regulate the band structure and broaden the light absorption range, but also provide active sites for photocatalytic reactions, enhancing the adsorption and conversion of reactants. Xian et al. [22]verified that the surface oxygen vacancy (OV) concentration of lead bismuth oxychloride ($PbBiO_2Cl$) can effectively adjust the intensity of the internal electric field, promote the transfer and separation of primary photogenerated charges, and thus enhance the selective CO_2 photoreduction. The high concentration of oxygen vacancies enhances the internal electric field and concurrently provides quantum wells for photogenerated electron trapping, thereby promoting efficient charge separation.

Conjugated conductive polymers constitute a unique class of organic semiconductor photocatalysts. Their extended π-conjugated systems facilitate extensive electron delocalization, resulting in high metallic-like conductivity and superior photoelectric properties [23]. Among them, polyaniline (PANI) has emerged as a promising candidate for large-scale applications due to its high conductivity, outstanding environmental stability, and convenient preparation [24,25]. Within the composite framework (specifically, PANI/semiconductor material), visible light excitation facilitates efficient electron injection from the PANI into the semiconductor conduction band [26], which effectively curtails the recombination of electron-hole pairs, consequently augmenting the photocatalytic performance of the hybrid material [27]. Qing et al. [28] reported that the C-PANI/Bi_3O_4Br heterojunction photocatalyst achieved rapid degradation of pollutants under visible light irradiation, with 100 % removal of E2 within 40 min and 100 % removal of RhB within 9 min. Similarly, Saddam et al. [29] successfully demonstrated that PANI, as a photosensitizer, can significantly improve the activity, enhance the charge transfer efficiency, and promote the separation of photogenerated carriers. The optimized NH_2-MIL-125@-PANI@Co_3O_4 photocatalyst remarkably enhanced the photocatalytic activity of the system. The layered structure of Bi_3O_4Br and the conductivity of PANI are expected to achieve the effective separation and transfer of photogenerated charges through the heterojunction structure, thereby improving the photocatalytic performance. Nevertheless, the regulation law of the photocatalytic efficiency and oxidation mechanism of the Bi_3O_4Br/PANI composite with the coupling structure of oxygen vacancies/heterojunction remains unclear and requires further exploration and evaluation.

Herein, in this study, the Bi_3O_4Br/PANI heterojunction photocatalyst was successfully fabricated via a simple hydrothermal method. The visible-light photocatalytic activity was evaluated by degrading CQP, and the key role of the oxygen vacancy/heterojunction coupling structure in enhancing the photocatalyst performance was further revealed in combination with the kinetic model. Simultaneously, the stability and activity changes of the photocatalyst under the influence of multiple environmental factors were also evaluated. This study also employed various in-situ/ex-situ characterizations to analyze the active species and degradation mechanism, as well as further combined toxicological simulation methods to propose the detoxification effect within the system.

2. Materials and methods

2.1. Catalysts fabrication

2.1.1. Preparation of Bi_3O_4Br nanosheets

2.91 g of $Bi(NO_3)_3$•$5H_2O$ and 2.40 g of polyvinylpyrrolidone (PVP) were dissolved in 200 mL mannitol solution (0.1 mM) with stirring for 30 min. Then, this mixture was treated dropwise with 40 mL of 1 mM NaBr, followed by 30 min of vigorous stirring. The pH was adjusted to 11.5 using NaOH, and the mixture was transferred to a reaction autoclave and heated at 160 °C for 24 h. Finally, the resulting Bi_3O_4Br nanosheets were collected by centrifugation, washed three times with deionized water and dried at 60 °C for 8 h.

2.1.2. Preparation of PANI/Bi_3O_4Br heterojunction

A certain mass of polyaniline (PANI) powder was dispersed in 200 mL of mannitol solution (0.1 mM). After 30 min of stirring, $Bi(NO_3)_3$•$5H_2O$ (2.91 g) and PVP (2.40 g) were added, and then 40 mL NaBr solution (1 mM) was dropped into the above mixture. The pH was adjusted to 11.5 using NaOH, and the mixture was transferred to a reaction autoclave and heated at 160 °C for 24 h. The resulting PANI/Bi_3O_4Br heterojunctions were collected by centrifugation, washed three times with deionized water and dried at 60 °C for 8 h. The mass ratios of PANI to Bi_3O_4Br were set to 0.025 %, 0.05 %, 0.1 %, and 0.2 %, which were designated as BBP-0.025 %, BBP-0.05 %, BBP-0.1 %, and BBP-0.2 %, respectively. The detailed preparation parameters for the BBP-X nanosheets are summarized in Table S1.

2.1.3. Preparation of oxygen vacancy-free BBP-0.05 % sample

As a control sample, 0.5 g of the synthesized BBP-0.05 % sample was dispersed in 20 mL of H_2O and hydrothermally treated at 140 °C for 3 h. The sample was then centrifuged, washed three times with deionized water, and dried at 60 °C for 8 h. The resulting material was oxygen-vacancy-free 0.05 % PANI/Bi_3O_4Br catalyst, which designated as BBP-noOV.

Similarly, when replacing BBP-0.05 % with pure Bi_3O_4Br nanosheets in the above process, the oxygen vacancy-free Bi_3O_4Br sample was obtained and denoted as Bi_3O_4Br noOV.

2.2. Photocatalytic activity measurement

For typical photocatalytic degradation experiments, 300 mg of photocatalyst was dispersed in 100 mL of a 0.5 mg/L CQP solution and sonicated for 1 min to ensure uniform dispersion, The suspension was then transferred to a 300 W xenon lamp reactor (Beijing Perfectlight, PLS-SXE300D) with a 12 cm distance between the light source and the liquid surface, maintaining a light intensity of 0.99 W/cm² at the surface. Prior to illumination, the suspension was stirred in the dark for 7 min to achieve adsorption-desorption equilibrium between the catalyst and the reactant. Photocatalytic degradation was initiated by turning on the xenon lamp, maintaining the reactor temperature at 25 °C. At predetermined intervals, 2 mL aliquots of the suspension were withdrawn, filtered through a 0.22 μm filter, and analyzed to determine the concentration of remaining pollutants. The concentration of CQP was analyzed by the UPLC system (Waters, ACQUITY UPLC H—CLASS) with a UV detector at wavelength of 342 nm and a BEH—C18 column. The mobile phase consisted of a mixture of acetonitrile to 0.3 % triethylamine at 10:90, and adjusted the flow rate to 0.25 mL/min.

Besides, the chemical reagents required, the characterizations and photocatalytic activity measurement were detailed displayed in Supporting Information.

3. Results and discussion

3.1. Characteristics

The crystal structures and phase constitutions of the BBP-X nanosheets were analyzed by X-ray diffraction (XRD) and Fourier-transform infrared (FTIR) spectroscopy. Fig. 1a shows that the pure PANI sample exhibits a broad peak characteristic of an amorphous structure. In contrast, the XRD pattern of the BBP-0.05 % sample clearly shows characteristic peaks at 23.9°, 28.2°, 29.0°, 31.4°, 38.0°, 39.7°, 42.8°, 45.0°, and 53.5°, corresponding to the (112), (006), (114), (020), (008), (206), (123), (220), and (033) planes of orthorhombic Bi_3O_4Br (JCPDS

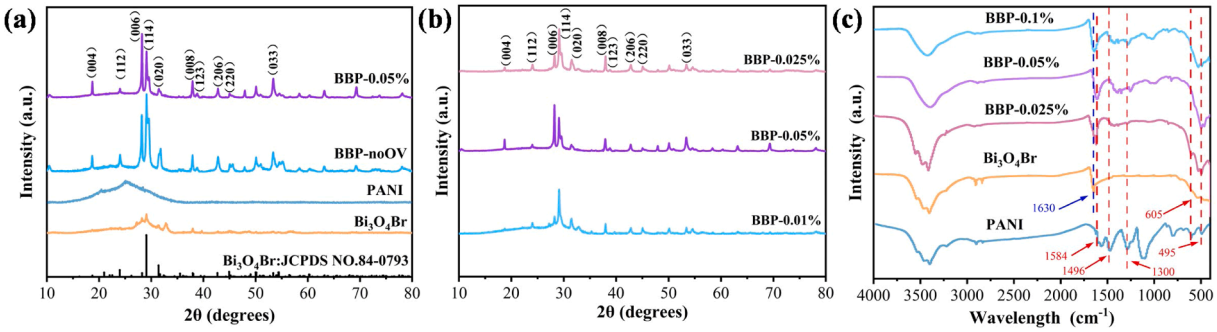

Fig. 1. XRD patterns of as-prepared PANI, Bi_3O_4Br, BBP-0.05 %, BBP-noOV catalysts (a) and BBP-X catalysts (b), Raman spectra of PANI, Bi_3O_4Br, and BBP-X (c).

84–0793), respectively [30]. These characteristic peaks are also observed in the BBP-noOV pattern, indicating that the removal of oxygen vacancies barely alter the crystal structure. Fig. 1b presents the XRD patterns of a series of BBP-X samples, all exhibiting clear Bi_3O_4Br characteristic peaks. With increasing PANI content, no new peaks besides those of Bi_3O_4Br are observed, attributable to the weak

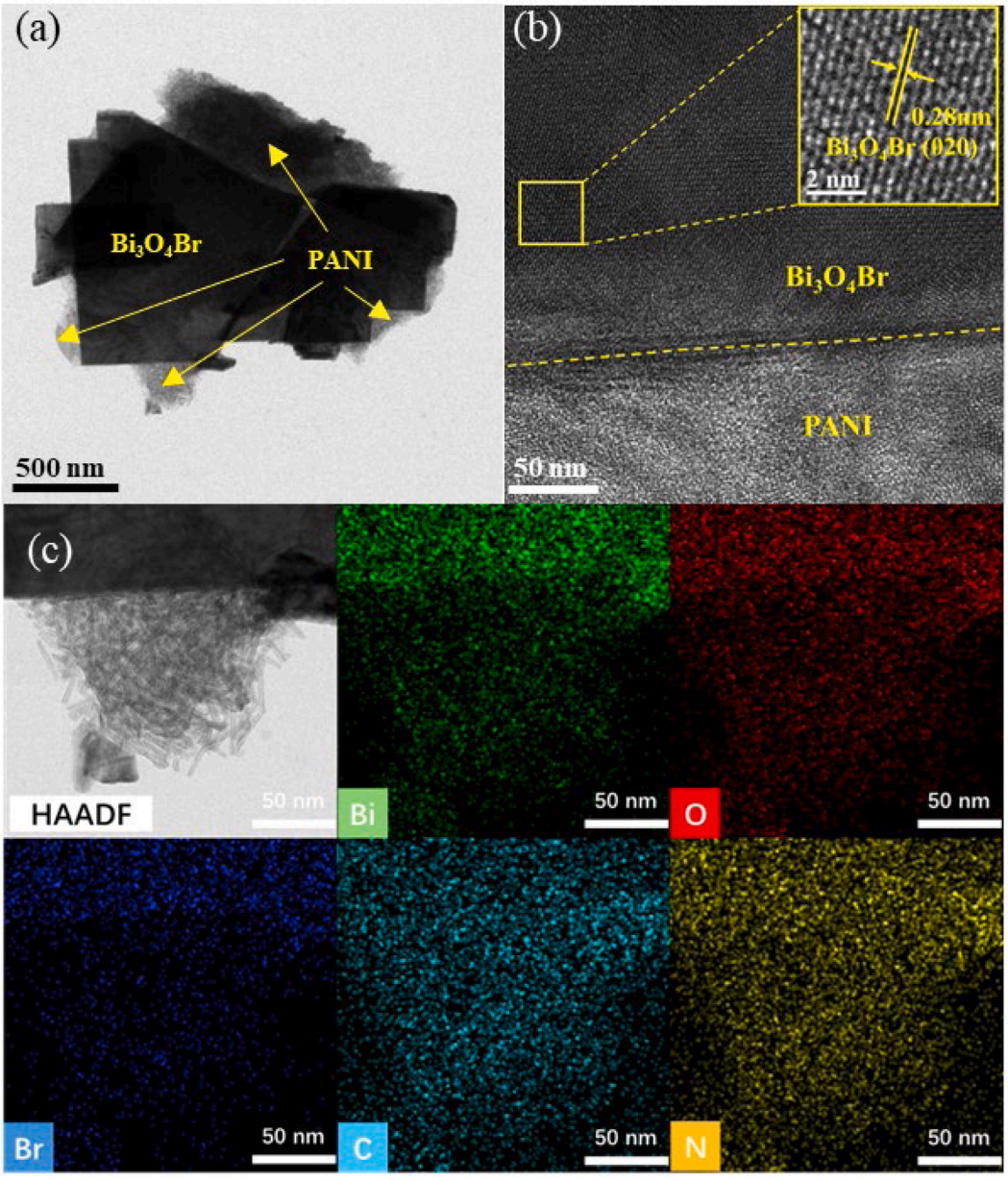

Fig. 2. SEM images of PANI/Bi_3O_4Br heterojunction (a), HRTEM image of BBP-0.05 % at 5 nm, where the yellow line indicates interface of PANI and Bi_3O_4Br (b), elemental mapping images of PANI/Bi_3O_4Br heterojunction at 50 nm (c).

crystallinity of PANI. Fig. 1c shows that the pure Bi_3O_4Br sample exhibits a strong absorption peak at 1630 cm^{-1}, assigned to the Bi-O stretching vibration. The FTIR spectrum of pure PANI shows strong peaks at approximately 1584 cm^{-1} and 1496 cm^{-1}, corresponding to the stretching vibrations of quinoid and benzenoid rings, respectively. The peak at 1300 cm^{-1} is attributed to the C—N stretching mode of the benzenoid units, while the characteristic absorption peaks at 605 cm^{-1} and 617 cm^{-1} are assigned to the C—N stretching vibration and in-plane bending vibration of the C—H bonds in the benzene rings of PANI, confirming the presence of PANI [31]. The FTIR spectra of the BBP-X composites are similar to that of pure Bi_3O_4Br, and with increasing PANI loading, the intensity of the characteristic PANI peaks increases. This observation confirms the successful formation of the BBP-X catalyst as a composite of PANI and Bi_3O_4Br.

Transmission electron microscopy (HRTEM) was employed to elucidate the surface morphology of PANI/Bi_3O_4Br composite. Fig. S2 and Fig. S3b shows the clustered nanoparticle morphology of PANI aggregates, Fig. 2a and Fig. S3a reveals that Bi_3O_4Br exhibits a distinct sheet-like structure, while densely packed PANI coats the Bi_3O_4Br plates, displaying an irregular aggregated morphology. As revealed by Fig. S3c and Fig. S3d, Bi_3O_4Br nanosheets are uniformly coated on the exterior surface of polyaniline (PANI), forming the BBP-0.05 % heterojunction and BBP-noOV counterpart, with no significant morphological alterations observed between these two samples. The formation of the Bi_3O_4Br nanosheets is attributed to a PVP-mediated self-assembly process. Through strong coordination with Bi^{3+} ions and interactions with the O and N atoms of pyrrolidone ring, PVP effectively passivates the Bi_3O_4Br surface, thereby arresting crystal growth [32]. Furthermore, steric hindrance arising from the polyethylene backbone of PVP restricts the anisotropic growth of Bi_3O_4Br along the c-axis. High-resolution imaging (Fig. 2b) clearly delineates the heterojunction interface of PANI/Bi_3O_4Br composites. Above the interface, distinct lattice fringes with an interplanar spacing of 0.28 nm are observed, unequivocally indexed to the (020) plane of Bi_3O_4Br. Conversely, the region below the interface displays amorphous characteristics, devoid of discernible lattice fringes, which is consistent with the PANI phase [33]. The intimate interfacial contact between the crystalline Bi_3O_4Br and amorphous PANI without discernible intermixing, provides compelling evidence for the successful fabrication of the PANI/Bi_3O_4Br heterojunction. EDS-mapping (Fig. 2c) confirms the homogeneous distribution of C, N, Bi, O, and Br throughout the composite, precluding any significant phase segregation [28].

X-ray photoelectron spectroscopy (XPS) was employed to investigate the valence states and surface chemical composition of the PANI/Bi_3O_4Br composite. The survey XPS spectrum (Fig. 3a) confirms the presence of Br, O, Bi, C, and N, consistent with EDS-mapping results. Deconvolution of the O 1 s spectrum (Fig. 3b) for pristine Bi_3O_4Br reveals three components: lattice oxygen at 529.3 eV, surface oxygen species (including oxygen vacancies and surface hydroxyl groups) at 530.8 eV, and adsorbed water at 532.5 eV, respectively. In the BBP-0.05 % composite, a slight blue shift of the O 1 s peaks are observed, attributable to the interfacial interaction of heterojunction. Meanwhile, the comparative analysis of BBP-0.05 % and BBP-noOV reveals a significant difference in the relative abundance of surface oxygen, with BBP-0.05 % exhibiting 61 % surface oxygen compared to only 49 % in BBP-noOV, which implies a higher concentration of oxygen vacancies in the BBP-0.05 % sample. Electron paramagnetic resonance (EPR) spectroscopy (Fig. 3c) was utilized to quantify oxygen vacancies. A prominent symmetric peak at $g = 2.002$ is clearly observed in the BBP-0.05 % sample, with its intensity surpassing those of samples with other concentrations, confirming a high concentration of oxygen vacancies on its surface. Conversely, this signal is absent in the BBP-noOV sample, corroborating the XPS findings. High-resolution Bi 4f XPS spectra (Fig. 3d) show characteristic peaks for pristine Bi_3O_4Br at 158.6 eV (Bi $4f_{7/2}$) and 164.0 eV (Bi $4f_{5/2}$), corresponding to Bi^{3+} [34–36]. In both BBP-0.05 % and BBP-noOV, these peaks exhibit a binding energy shift to lower values (158.1 eV and 163.4 eV for BBP-0.05 %; 158.4 eV and 163.7 eV for BBP-noOV), which indicate that both heterojunction formation and rich oxygen vacancies contribute to the reduction of Bi binding energy. Similarly, in the XPS spectrum of Br 3d (Fig. 3e), two peaks are observed at 69.0 eV and 67.9 eV for pristine Bi_3O_4Br, corresponding to the $3d_{3/2}$ and $3d_{5/2}$ orbitals of Br^-, respectively. In BBP-0.05 %, a slight shift of the Br peaks to lower binding energies (68.5 eV and 67.4 eV) is observed, likely due to the synergistic effects of heterojunction formation and oxygen vacancies [30,35]. The N 1 s high-resolution XPS spectrum (Fig. 3f) for pristine PANI exhibits two peaks attributed to –NH– groups

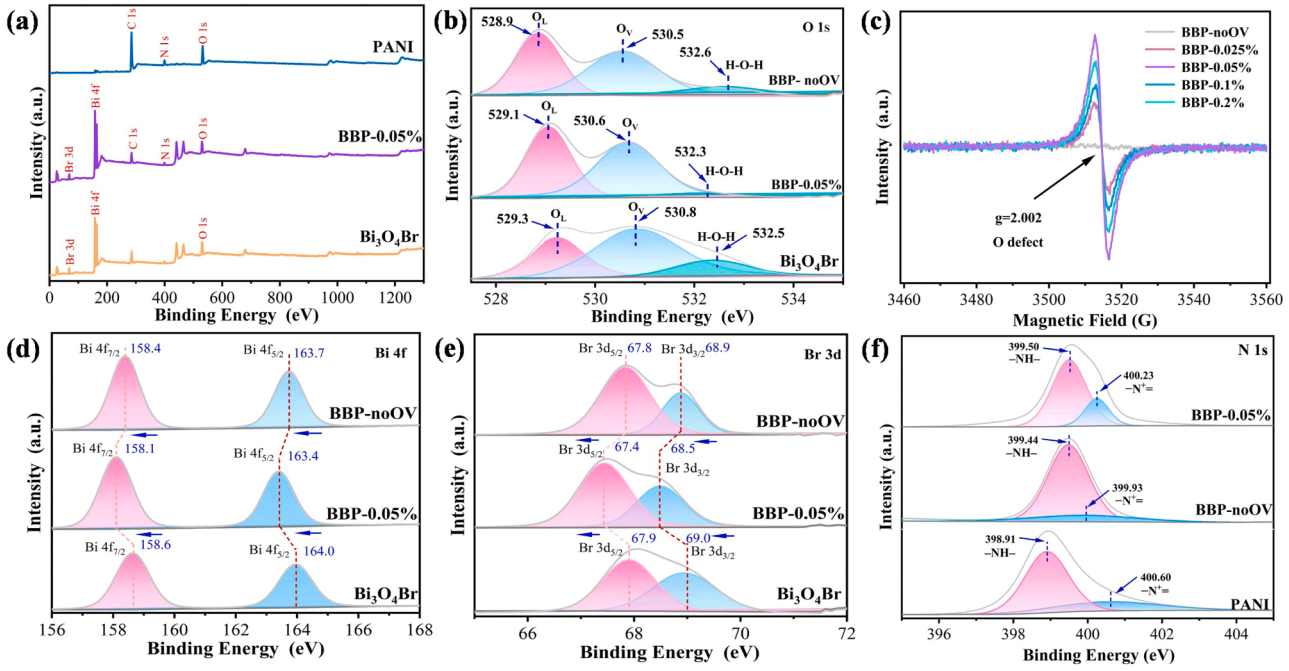

Fig. 3. Survey XPS spectra of the as-prepared PANI, Bi_3O_4Br and BBP-0.05 % (a), XPS spectra of O 1 s (b), ESR spectra (c), Bi 4f (d) and Br 3d (e) of BBP-noOV, BBP-0.05 %,and Bi_3O_4Br, and N 1 s XPS spectra of BBP-noOV, BBP-0.05 % and PANI (f).

(398.91 eV) and positively charged nitrogen (400.60 eV). Compared to pristine PANI, the –NH– peak in BBP-0.05 % displays a red shift due to electron delocalization between the Bi p orbitals and the π-conjugated ligands of PANI [37]. The N electrons in PANI are efficiently injected into the conduction band of Bi_3O_4Br semiconductor. Moreover, the relative intensity of the positively charged nitrogen peak increases. These observations suggest a partial electron loss from N atoms upon heterojunction formation. Collectively, the observed binding energy shifts of Br, Bi, N, and O peaks strongly demonstrate the existence of built-in electric field between PANI and Bi_3O_4Br within the heterojunction, which is further enhanced by the high concentration of oxygen vacancies.

3.2. Catalytic performance

3.2.1. Degradation kinetics

The visible-light photocatalytic performances of BBP-X heterojunction were evaluated using CQP as a probe pollutant. As shown in Fig. 4a, after 7 min of dark adsorption, the adsorption of CQP in all five reaction systems were below 10 %, indicating relatively weak adsorption capacities of these catalysts. Under visible-light irradiation for 3 min, pure PANI and Bi_3O_4Br degraded only approximately 15 % and 60 % of CQP, respectively, demonstrating limited photocatalytic activity [38]. Noteworthy, BBP-0.05 % achieved 55 % CQP degradation within just 30 s of the photocatalytic reaction, reaching 85 % after 1 min and exceeding 95 % after 2 min. The significantly enhanced photocatalytic performance highlighted the crucial role of the heterojunction [39]. Furthermore, the control samples without oxygen vacancies (Bi_3O_4Br noOV and BBP-noOV) degraded only 10 % and 20 % of CQP within 7 min, respectively. This clearly demonstrated the critical role of oxygen vacancies in the photocatalytic reaction, representing another crucial factor in enhancing photocatalytic activity. A first-order kinetic model was employed to calculate the rate constants (k) for CQP degradation by different catalysts (Fig. 4b and S4). As shown in Fig. 4b, the rate constants (k) for PANI, Bi_3O_4Br, BBP-0.05 %, Bi_3O_4Br noOV, and BBP-noOV were 0.0416, 0.2424, 1.1586, 0.0175, and 0.0402 min^{-1}, respectively. The k value of BBP-0.05 % was 23 and 5 times higher than those of PANI and Bi_3O_4Br, respectively, while the k values of Bi_3O_4Br and BBP-0.05 % with rich oxygen vacancies were 14 and 25 times higher than their counterparts without oxygen vacancies. These results strongly demonstrated the superior photocatalytic efficiency of the oxygen-vacancy-rich PANI/Bi_3O_4Br heterojunction, where the synergistic effect of the heterojunction and oxygen vacancies played a pivotal role.

To determine the optimal composite ratio of PANI and Bi_3O_4Br, a series of BBP-X composites were prepared by adjusting the PANI loading, and their photocatalytic performance was evaluated (Fig. 4c). Under dark conditions, all BBP-X samples exhibited weak CQP adsorption. After 3 min irradiation, BBP-0.025 % achieved 78 % CQP removal, and the removal efficiency peaked at 95 % with a PANI loading of 0.05 % [40]. However, further increasing the PANI loading to 0.1 % and 0.2 % resulted in a gradual decrease in removal efficiency to 74 % and 69 %, respectively. First-order kinetic modeling (Fig. 4d) revealed that BBP-0.05 % exhibited the highest rate constant, which was 2.7, 2.9, and 3.6 times greater than those of BBP-0.025 %, BBP-0.1 %, and BBP-0.2 %, respectively. These results indicated a significant influence of PANI loading on the catalytic efficiency of the heterojunction, with 0.05 wt % identified as the optimal loading. Consequently, BBP-0.05 % was used in subsequent studies. To further explore its applicability, the reusability and stability of BBP-0.05 % were investigated under identical conditions. As shown in Fig. S5a-b, after three cycles of experiments, the photocatalytic activity of BBP-0.05 % decreased slightly, and the degradation efficiency within 7 min was still 80 %, indicating that BBP-0.05 % has good recyclability. Meanwhile, XRD spectra, FTIR spectra and EDX mapping analysis were used to explore the stability of BBP-0.05 %. As shown in Fig. S5c-d and S6, there was no significant change in BBP-0.05 % before and after the reaction, demonstrating the excellent stability in the morphology and crystal structure of BBP-0.05 % [41]. As evidenced in Fig. S7, in the BBP-0.05 % system, approximately 43 % of the organic carbon was completely mineralized into inorganic carbon. In contrast, the TOC removal efficiencies in the PANI, Bi_3O_4Br,

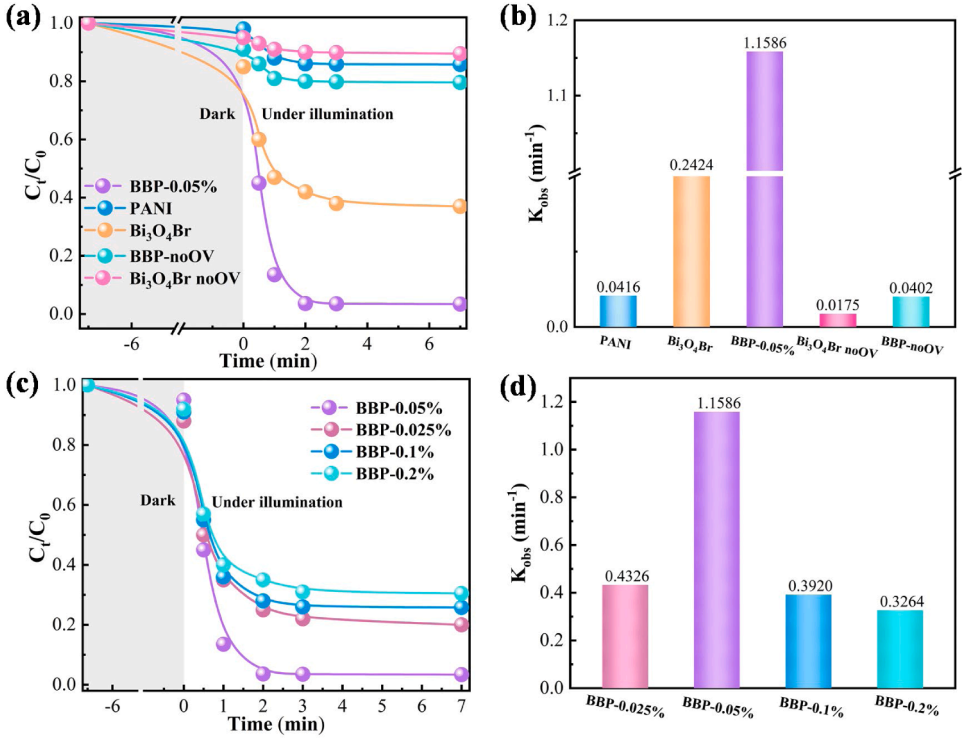

Fig. 4. Photocatalytic degradation curves of CQP with different catalysts (a), corresponding reaction rate constants (b), photocatalytic degradation curve of CQP by BBP-X (c), reaction rate constants of BBP-X for CQP (d). (Reaction conditions: Temperature = 298 K, initial pH= ±7.0, [CQP] = 1 mg/L, Catalysts = 3 g/L.).

Bi_3O_4Br noOV, and BBP-noOV systems were only 22 %, 31 %, 12 %, and 20 %, respectively. These results demonstrate that the BBP-0.05 % sample exhibits superior photocatalytic performance, enabling the complete degradation of approximately half of the CQP in the system and its conversion into inorganic matter and water.

3.2.2. Specific surface area analysis

Initially, the specific surface areas of various samples (BBP-0.05 %, BBP-noOV, Bi_3O_4Br, and PANI) were investigated, with results summarized in the corresponding table (Fig. S9 and Table S5). BET analysis confirmed specific surface areas of 40.365 m^2/g (BBP-0.05 %), 42.351 m^2/g (BBP-noOV), 36.233 m^2/g (Bi_3O_4Br), and 26.087 m^2/g (PANI). Although high surface area typically correlates with enhanced catalytic activity through increased active site exposure, normalization of initial reaction kinetic constants (k_S) revealed critical insights. BBP-0.05 % exhibited a normalized k_S value of 57.406×10^{-3} $min^{-1}\cdot L\cdot m^{-2}$, surpassing those of BBP-noOV (1.898×10^{-3} $min^{-1}\cdot L\cdot m^{-2}$), Bi_3O_4Br (13.384×10^{-3} $min^{-1}\cdot L\cdot m^{-2}$), and PANI ($3.189 \times 10^{-3}$ $min^{-1}\cdot L\cdot m^{-2}$) by factors of 30.2, 4.3, and 18.0, respectively. This substantial disparity in surface area-normalized kinetics conclusively demonstrates that specific surface area contributes minimally to the exceptional photocatalytic performance of BBP-0.05 %, excluding it as the primary driver of activity enhancement.

3.2.3. Influence of environmental factors

Fulvic acid (FA), a ubiquitous natural organic matter (NOM) in aquatic environments, can compete for catalytic active sites and inhibit the generation of reactive oxygen species (ROS). The quinone groups in FA can consume the energy of photoexcited catalysts, interfere with energy transfer processes, and thereby reduce the generation of $^1O_2$, thereby suppressing photocatalytic degradation processes [42]. This section investigates the effect of FA on the CQP degradation efficiency in the BBP-0.05 %/Vis system. As shown in Fig. 5a, when the FA concentration was 1.0, 10, and 20 mg l^{-1}, the removal efficiency of CQP by BBP-0.05 % after 7 min irradiation exhibited an obvious downward trend, reaching 90.0 %, 72.0 %, and 59.0 %, respectively. Concurrently, the pseudo-first-order kinetic rate constant (k) decreased significantly from 1.156 min^{-1} to 0.1997 min^{-1} (Fig. S8a). These results clearly demonstrated a marked influence of FA presence on the photocatalytic oxidation efficiency, which was likely attributable to the quenching of ROS and the competition between FA and CQP for active sites on the catalyst surface as FA concentration increased. This competitive mechanism further inhibited the CQP oxidation process, thus reducing its degradation efficiency.

Bicarbonate ions, chloride ions and sulfate ions are anions that commonly exist in the water environment. Previous studies have shown that these anions can affect the photodegradation efficiency during the water treatment process. Therefore, this study focused on exploring the specific impacts of SO_4^{2-}, Cl^- and HCO_3^- on the BBP-0.05 % photocatalytic system. Fig. 5b illustrated that the CQP removal efficiency of BBP-0.05 %/Vis within 7 min was 97.2 %, 85.0 %, 80.0 %, and 77.0 % under 0, 1, 5, and 10 μM SO_4^{2-} conditions, respectively. This slight inhibitory effect was likely due to the hydroxyl radical (•OH) scavenging ability of sulfate ions. SO_4^{2-} outcompete target contaminants (CQP) for surface adsorption on catalysts, occupying spatially confined reactive sites or obstructing electron transport channels, which compromises the accessibility of pollutants to active catalytic centers [43]. As shown in Fig. 5c, the catalytic performance of BBP-0.05 % exhibited a more pronounced fluctuation under the influence of Cl^-. After adding 1, 5, and 10 μM Cl^-, the CQP removal efficiency within 7 min decreased to 79.0 %, 62.0 %, and 50.0 %, respectively. Correspondingly, the pseudo-first-order kinetic constant (k) significantly decreased from 1.156 min^{-1} to 0.1818 min^{-1}, indicating that the reaction rate was affected to a certain extent (Fig. S8c). This was primarily attributed to the ability of Cl^- ions to scavenge ·OH and the competition between Cl^- and CQP for active sites on the surface of the BBP-0.05 % photocatalyst. Cl^- exhibit preferential scavenging of photogenerated electrons (e^-), thereby impeding their involvement in dissolved oxygen reduction to generate reactive intermediates such as superoxide radicals ($•O_2^-$) or hydroxyl radicals (•OH) [44]. Similarly, HCO_3^- also affected the efficiency of photocatalytic CQP degradation (Fig. 5d). Under co-existing conditions of 1, 5, and 10 μM HCO_3^-, the CQP removal efficiency of BBP-0.05 % within 7 min decreased to 90.0 %, 70.0 %, and 62.0 %, respectively. This could be attributed to the quenching of h^+ by bicarbonate ions, where h^+ played a

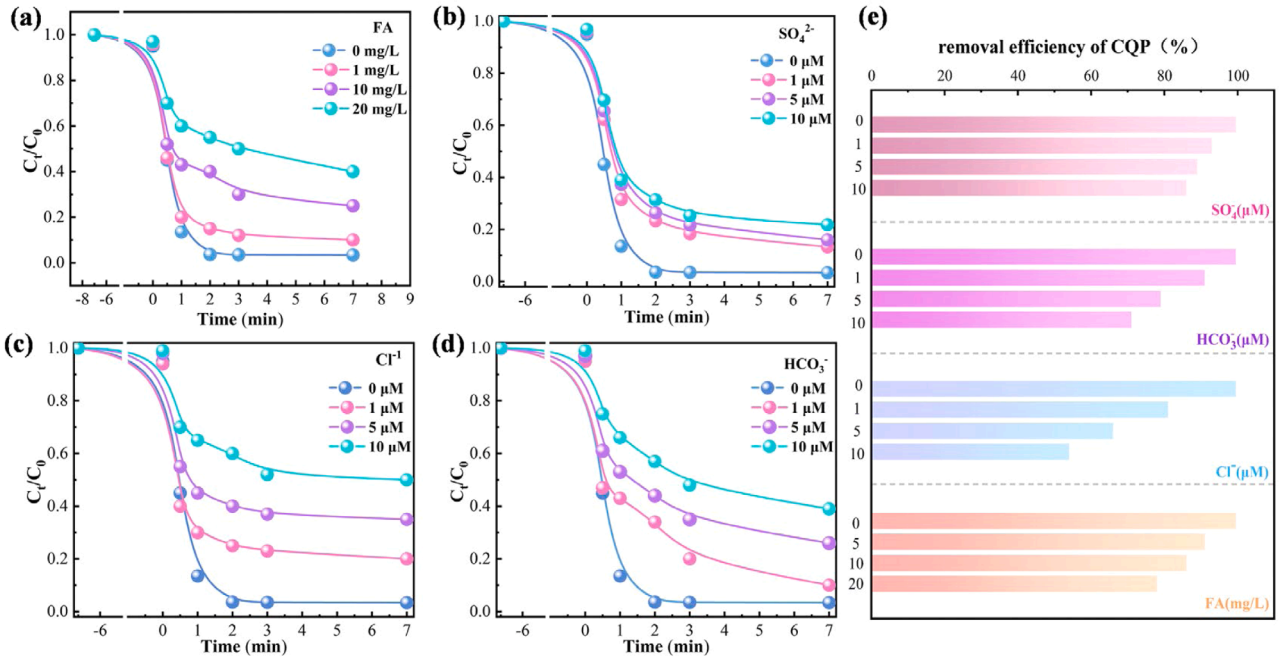

Fig. 5. Influences of different operational parameters on BBP-0.05 % photocatalytic system: FA (a), SO_4^{2-} (b), Cl^- (c), HCO_3^- (d), and the removal rate of CQP by BBP-0.05 % under different concentrations of FA, SO_4^{2-}, Cl^- and HCO_3^- (e). (Reaction conditions: Temperature = 298 K, initial pH= ±7.0, [CQP] = 1 mg/L, Catalysts = 3 g/L.).

crucial role in the reaction system. HCO_3^- induce the formation of surface-bound recombination centers via strong chemisorption on heterojunction catalysts, accelerating the recombination of photogenerated electrons (e^-) and holes (h^+), thereby preventing h^+ from effectively participating in direct oxidation reactions of pollutants [45]. These experimental results indicated that the BBP-0.05 % system still exhibited excellent CQP removal efficiency under the co-existence of low concentrations of FA and anions. However, under high concentrations of background substances, the removal efficiency slightly decreased, although it still effectively removed >50 % of CQP.

3.3. Structure-activity relationship analysis

3.3.1. Band structure

To gain a deeper understanding of the band structure characteristics of the BBP-0.05 % composite material, valence band X-ray photoelectron spectroscopy (VB-XPS) and UV–Vis diffuse reflectance spectroscopy (UV–Vis DRS) were employed to analyze the visible-light absorption capacity and band structure. As shown in Fig. 6a, all photocatalysts exhibited excellent light absorption capabilities in the wavelength range above 400 nm, indicating their effective excitation by visible light. Compared to pure Bi_3O_4Br, the BBP-0.05 % composite material showed a significant red shift in its light absorption edge and enhanced absorption intensity, which demonstrated that introducing PANI into heterojunction effectively broadened the range of light absorption. Furthermore, compared to BBP-noOV, the light absorption edge of BBP-0.05 % also exhibited a noticeable red shift, further confirming the contribution of abundant oxygen vacancies to enhanced light absorption. The band gap (Eg) energies of PANI and Bi_3O_4Br were calculated using the Kubelka-Munk function, resulting in values of 2.46 eV and 2.29 eV, respectively (Fig. 6b). Their valence band (or HOMO) energy levels were determined using VB-XPS spectroscopy. As shown in Figure S10, the valence band (VB or HOMO) energy levels of PANI and Bi_3O_4Br were 1.48 eV and 1.06 eV, respectively. Based on the energy level equation $Eg = E_{CB} + E_{VB}$, the LUMO potential of PANI and the conduction band (CB) potential of Bi_3O_4Br were further calculated to be −0.98 eV and −1.23 eV, respectively. Based on these experimental results, a relative band position diagram for PANI and Bi_3O_4Br was constructed (Fig. 6c) [26]. It clearly depicted that the E_{CB} level of PANI was significantly lower than that of Bi_3O_4Br, while the E_{VB} position of PANI was higher than that of Bi_3O_4Br. This staggered band structure was a sufficient condition for heterojunction formation [46].

3.3.2. Photoelectrochemical properties analysis

Beyond light absorption, the efficiency of photogenerated charge carrier separation and migration is another crucial factor for photocatalytic activity. Fig. 7a presented the photoluminescence (PL) spectra of different catalysts, where the characteristic emission peak of all samples appeared at approximately 490 nm. Compared to BBP-noOV, the fluorescence peak intensity of BBP-0.05 % was significantly lower, indicating that the photogenerated charge carrier recombination rate of BBP-0.05 % was considerably lower than that of BBP-noOV. This result confirmed that the presence of oxygen vacancies effectively suppressed the recombination of photogenerated electrons (e^-) and holes (h^+), thus benefiting the photocatalytic reaction [47]. Furthermore, the peak intensity of BBP-0.05 % was observed to be greater than that of pure Bi_3O_4Br and PANI, which was attributed to the significantly lower number of photogenerated charge carriers in the pure Bi_3O_4Br and PANI sample, resulting in a weaker PL signal [48].

To further investigate the photoinduced charge separation and migration efficiency, as well as the interfacial charge transfer resistance of the BBP-0.05 % composites, linear sweep voltammetry (LSV) measurements were performed in a three-electrode system using a 0.05 M Na_2SO_4 solution (Fig. 7b-c). The results showed that the photocurrent intensity of the BBP-0.05 % was significantly higher than that of pure Bi_3O_4Br and approximately three times that of PANI, indicating that the charge separation efficiency was superior to that of the single components after heterojunction formation. Maximum photocurrent intensity was observed at a 0.05 % PANI loading. Meanwhile, the photocurrent of BBP-0.05 % sample was also significantly higher than that of BBP-noOV, again confirming that oxygen vacancies enhanced charge carrier separation and migration. Similarly, Nyquist plots from electrochemical impedance spectroscopy (EIS) (Fig. 7d-e) demonstrated that the BBP-0.05 % composite exhibited substantially lower charge transfer resistance than single-component materials or heterojunctions with alternative PANI loadings [49]. These findings correlated directly with the enhanced photocatalytic degradation observed [50]. Furthermore, time-resolved photoluminescence (TRPL) spectroscopy (Fig. 7f) indicated that the heterojunction structure in BBP-0.05 % promoted efficient non-radiative recombination pathways, resulting in a shorter average carrier lifetime (1.095 ns) compared to pure Bi_3O_4Br (1.224 ns), PANI (1.157 ns), and BBP-noOV (1.160 ns). This accelerated electron transfer from Bi_3O_4Br to PANI suppressed charge carrier recombination, thereby enhancing the photocatalytic efficiency. The presence of oxygen vacancies further contributed to this effect [51,52].

3.4. Catalytic oxidation mechanism

3.4.1. Identification of active species

Electron paramagnetic resonance (EPR) spectroscopy was employed to identify reactive oxygen species (ROS) generated within the BBP-0.05 %/Vis system. No EPR signals were detected in the absence of organic pollutants under dark conditions (Fig. 8a-b). However, upon illumination, a characteristic triplet signal (1:1:1 intensity ratio) emerged and its intensity increasing significantly from 0.5 to 3 min of irradiation, confirming the formation of singlet oxygen ($^1O_2$). This assignment was further supported by the observation that continuous purging of the system with nitrogen (TEMP+N_2 curve) substantially diminished this signal, indicating that dissolved oxygen served as the precursor for $^1O_2$ generation. Concurrently, using 5,5-dimethyl-1-pyrroline N-oxide (DMPO) as a spin trap in methanol, a six-line signal characteristic of the DMPO-•O_2^- adduct was observed upon illumination (Fig. 8c), confirming

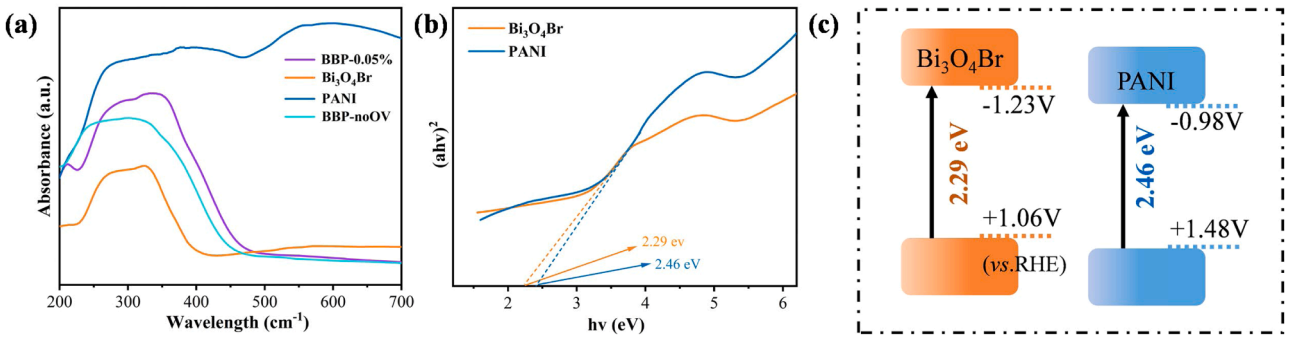

Fig. 6. UV–vis diffuse reflection spectra (a), the bandgap values calculated from Kubelka-Munk plots (b), band gap diagram (c).

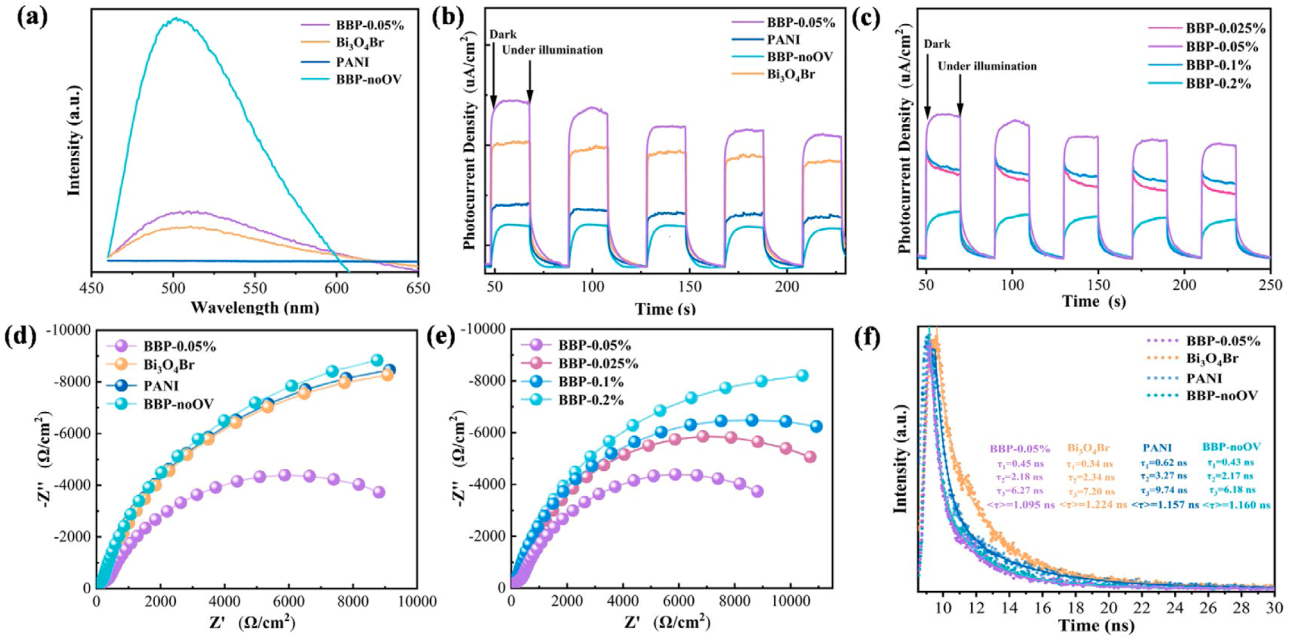

Fig. 7. PL spectra (a), transient photocurrent response spectra (b-c), electrochemical impedance spectra (d-e) and time-resolved fluorescence spectroscopy (f) of as-prepared samples. (Reaction conditions: Temperature =298 K, initial pH=±7.0, [CQP] =1 mg/L, Catalysts =3 g/L.

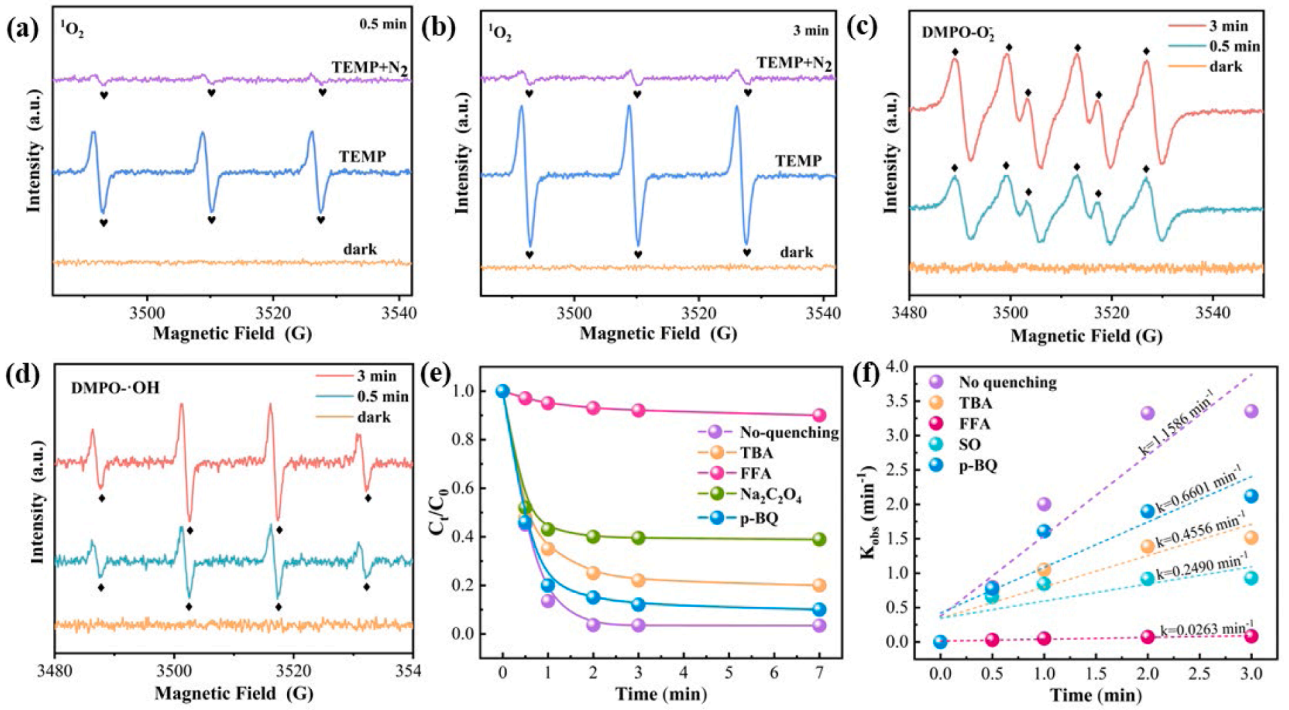

Fig. 8. TEMP-$^1O_2$ formation after 30 s (a) and 3 min (b) illumination, EPR spectra obtained with addition of DMPO-•O_2^- (c) and DMPO-•OH (d); quenching effect of different scavengers (e); determination of rate constants in CQP degradation quenching (f). (Reaction conditions: Temperature =298 K, initial pH=±7.0, [CQP] =1 mg/L, Catalysts =3 g/L, [TBA] = [FFA] = [$Na_2C_2O_4$] = [p-BQ] =10 mM, [TEMP] =1 mM [DMPO] =10 mM.).

the formation of superoxide radicals (•O_2^-) [53]. Similarly, in an aqueous DMPO system (Fig. 8d), illumination yielded a four-line signal (1:2:2:1 intensity ratio), consistent with the existence of hydroxyl radicals (•OH) [54].

To elucidate the roles of different reactive oxygen species (ROS) in the PANI/ Bi_3O_4Br-catalyzed photodegradation of CQP, quenching experiments were performed. Specifically, tert-butanol (TBA), p-benzoquinone (p-BQ), furfuryl alcohol (FFA), and sodium oxalate ($Na_2C_2O_4$) were employed as scavengers for •OH, •O_2^-, $^1O_2$, and h^+, respectively, at a concentration of 5 mM. As shown in Figs. 8e-f, the addition of these scavengers resulted in drops of CQP degradation efficiency from 95 % to 79 %, 9 %, 58 %, and 89 %, respectively, with corresponding decreases in the pseudo-first-order rate constant (k) to 0.4556, 0.0263, 0.2490, and 0.6601 min^{-1}. These results indicated the following order of ROS contribution to CQP degradation: $^1O_2$> h^+> •OH> •O_2^-. Therefore, while multiple ROS participated in the photocatalytic process, $^1O_2$ and

h^+ were identified as the dominant reactive species, with hydroxyl and superoxide radicals playing secondary roles.

3.4.2. Photocatalytic mechanism analysis

Based on the experimental results, the mechanism for the visible-light-driven photocatalytic degradation of CQP by the PANI/Bi_3O_4Br heterojunction was proposed (Fig. 9a). Visible light irradiation promoted electron transfer from the valence band (VB) to the conduction band (CB) in both PANI and Bi_3O_4Br, generating electron-hole pairs [55]. The presence of oxygen vacancies in Bi_3O_4Br facilitated the migration of photogenerated electrons from the CB of Bi_3O_4Br to the oxygen vacancy levels and subsequently to the lower-energy LUMO of PANI. Simultaneously, holes transferred from the HOMO of PANI to the VB of Bi_3O_4Br, driven by the heterojunction. This spatial charge separation effectively suppressed electron-hole recombination, enhancing photocatalytic activity. The significantly more negative LUMO potential of PANI (−0.84 V vs. NHE) compared to the $O_2/\bullet O_2^-$ redox potential (−0.33 V vs. NHE) enabled the reduction of dissolved oxygen to $\bullet O_2^-$, which subsequently reacted with water to produce $^1O_2$ and •OH. Furthermore, the photogenerated holes with oxidizing capacity in the Bi_3O_4Br VB also contributed significantly to the oxidation process.

$$^1O_2 + e^- \rightarrow \bullet O_2^- \quad (1)$$

$$4\bullet OH \rightarrow {}^1O_2 + 2H_2O \quad (2)$$

$$H^+ + \cdot\bullet OH + e^- \rightarrow H_2O \quad (3)$$

$$H_2O + h^+ \rightarrow OH^- + H \quad (4)$$

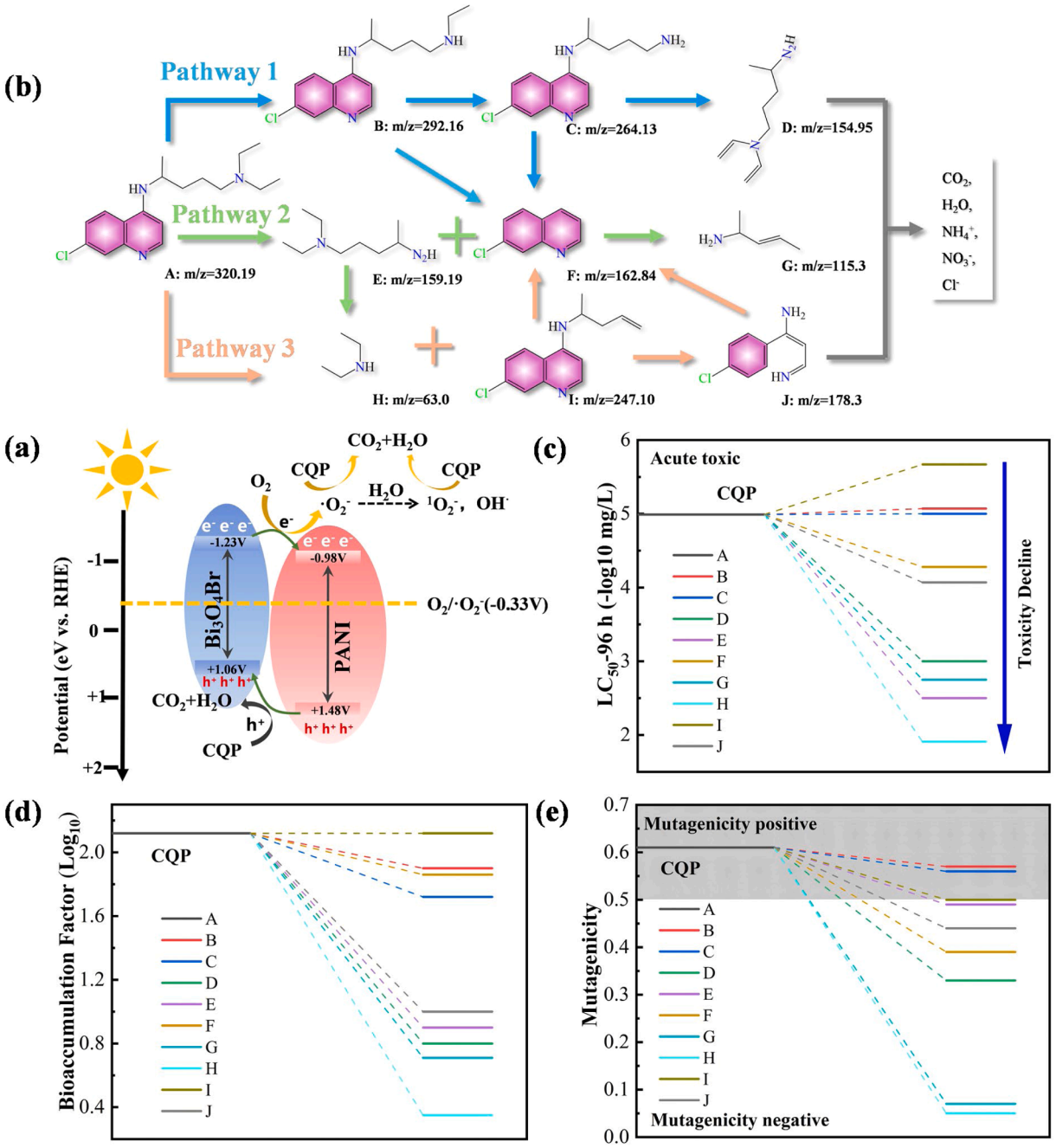

Fig. 9. Photocatalytic mechanism of CQP degradation in BBP-0.05 %/Vis system (a), possible CQP degradation pathway of BBP-0.05 %/Vis system(b). The toxicity of CQP and further degradation intermediates: daphnia magna LC_{50}–96 h (c), bioconcentration factor (d), and mutagenicity (e).

$$\bullet O_2^- + \bullet OH \rightarrow {}^1O_2 + OH^- \quad (5)$$

$$\bullet OH + Cl^- \rightarrow OH^- + Cl^{\cdot} \quad (6)$$

$${}^1O_2 + \cdot\bullet O_2^- + h^+ + CQP \rightarrow \text{intermediates} \rightarrow CO_2 + H_2O + NO_3^- + NH_4^+ + Cl^- \quad (7)$$

3.5. Degradation products and toxicological analysis

3.5.1. Degradation pathways

LC-MS/MS analysis was employed to identify CQP degradation intermediates generated in the BBP-0.05 %/Vis system, revealing three major degradation pathways (Fig. 9b). Pathway 1 involved initial terminal decarboxylation of CQP, yielding intermediate B ($m/z = 292.16$), which subsequently underwent further decarboxylation to form intermediates C ($m/z = 264.13$) and F ($m/z = 162.84$). Intermediate C then underwent C—H bond cleavage to produce the ring-opened product D ($m/z = 154.95$) and additional decarboxylation to yield F. Pathway 2 involved initial decarboxylation of CQP to yield intermediates E ($m/z = 159.19$) and F, then F underwent decarboxylation and ring opening to form G ($m/z = 115.30$), with E also producing H through decarboxylation. In Pathway 3, CQP underwent direct oxidation by $^1O_2$ and h^+ to yield H ($m/z = 63.00$) and I ($m/z = 247.10$), and I was further oxidized to the ring-opened product J ($m/z = 178.30$). Ultimately, all identified intermediates underwent further oxidation via decarboxylation, dechlorination, and denitrogenation pathways, yielding small, mineralized products including water, CO_2, NH_4^+, NO_3^-, and Cl^-.

3.5.2. Toxicological analysis of intermediates

To evaluate the potential environmental impact of the PANI/Bi_3O_4Br visible-light photocatalytic degradation of CQP, the acute toxicity, bioaccumulation potential, and mutagenicity of CQP and nine identified intermediates were assessed using the Toxicity Estimation Software Tool (T.E.S.T.) and quantitative structure-activity relationship (QSAR) modeling [56,57]. The LC_{50} value for CQP in fathead minnows was determined to be 4.98 ($-\log_{10}$ mg/L). Significantly, the LC_{50} values for intermediates B, C, D, E, F, G, and H were all lower than that of the parent compound CQP, indicating reduced acute toxicity (Fig. 9c). Furthermore, the bioaccumulation factors for all intermediates were lower than that of CQP (Fig. 9d), and mutagenicity was also reduced, with intermediates B, D, E, F, G, H, and J exhibiting no detectable toxicity (Fig. 9e). These findings demonstrated that the BBP-X heterojunction photocatalytic system not only effectively removed CQP but also mitigated its potential ecological impact.

4. Conclusion

In summary, this paper has successfully designed a Bi_3O_4Br/PANI heterojunction nanosheet catalyst with an oxygen vacancy-rich structure. By adjusting the loading amount of PANI, a controllable preparation scheme for the catalyst has been proposed. On this basis, taking chloroquine phosphate (CQP) as the target degradation substance, the photocatalytic activity of Bi_3O_4Br/PANI photocatalytic system was studied. Under visible light irradiation for 2 min, the prepared BBP-0.05 % nanosheets exhibited the optimal photocatalytic activity, with the degradation efficiency of CQP reaching above 95 %. The corresponding apparent rate constant (k) was as high as 1.15 min^{-1}, which was 4.8 times that of Bi_3O_4Br (0.242 min^{-1}) and 25 times that of BBP-noOV (0.01754 min^{-1}). Through a variety of photoelectric characterizations, it was found that the coupling structure of oxygen vacancy and heterojunction could effectively improve the visible light absorption ability and simultaneously form a built-in electric field to promote the separation and migration effects of photogenerated carriers, thereby significantly enhancing the photocatalytic performance. Quenching tests and ESR spectra indicated that non-radicals (singlet oxygen and holes) were the main pathways for the photocatalytic oxidation of CQP molecules. Meanwhile, combined with the intermediate products of CQP oxidation, the possible degradation pathways were proposed, mainly including C—N bond breaking, decarbonization, dechlorination, and denitrification. In addition, based on multiple toxicological simulations, it was demonstrated that the PANI/Bi_3O_4Br photocatalytic reaction system revealed a positive detoxification impact on the CQP elimination.

CRediT authorship contribution statement

Qiao Wang: Writing – original draft, Validation, Methodology, Funding acquisition, Formal analysis. **Yiwen Peng:** Writing – original draft, Visualization, Investigation, Data curation. **Aobo He:** Investigation, Data curation. **Zhenshen Li:** Investigation, Data curation. **Jialin Jia:** Writing – review & editing, Supervision, Conceptualization. **Huahong Xu:** Investigation, Data curation. **Yuemi Yu:** Investigation, Data curation. **Zhiqiang Zhang:** Writing – review & editing.

Declaration of competing interest

The authors declare that they have no known competing financial interests or personal relationships that could have appeared to influence the work reported in this paper.

Acknowledgements

The authors gratefully acknowledge the National Natural Science Foundation of China (Grant No 22006022) and the Natural Science Foundation of Jiangsu Province (Grant No BK20241535). We would like to thank Analysis and Test Center of Guangdong University of Technology for UPLC analysis.

Supplementary materials

Supplementary material associated with this article can be found, in the online version, at doi:10.1016/j.surfin.2025.106866.

Data availability

No data was used for the research described in the article.

References

[1] X. Yi, H. Ji, C. Wang, Y. Li, Y. Li, C. Zhao, A. Wang, H. Fu, P. Wang, X. Zhao, W. Liu, Photocatalysis-activated SR-AOP over PDINH/MIL-88A(Fe) composites for boosted chloroquine phosphate degradation: performance, mechanism, pathway and DFT calculations, Appl. Catal. B 293 (2021) 120229.
[2] H. Dai, W. Luo, L. Jin, L. Deng, Q. Wang, J. Hu, R.P. Singh, Degradation of chloroquine phosphate during UV/H_2O_2 process: performance, kinetics, and degradation pathways, J. Environ. Chem. Eng. 12 (2024) 112493.
[3] H. Peng, X. Shi, Z. Sun, ZIF-67-derived Co_3S_4-modified cathode with high Co^{II} content enhances the removal of chloroquine phosphate by the electro-fenton system, J. Water. Process. Eng. 63 (2024) 105526.
[4] F. Eisenreich, Photocatalysis as an effective tool for upcycling polymers into value-added molecules, Angew. Chem. Int. Ed. Engl. 62 (2023) e202301303.
[5] T. Lv, J. Li, N. Arif, L. Qi, J. Lu, Z. Ye, Y.-J. Zeng, Polarization and External-Field Enhanced Photocatalysis, 5, Matter-Us, 2022, pp. 2685–2721.
[6] V. Srivastava, P.K. Singh, P.P. Singh, Recent advances of visible-light photocatalysis in the functionalization of organic compounds, J. Photochem. Photobiol. C 50 (2022) 100488.
[7] M. Cai, Y. Liu, K. Dong, X. Chen, S. Li, Floatable S-scheme Bi_2WO_6/C_3N_4/carbon fiber cloth composite photocatalyst for efficient water decontamination, Chin. J. Catal. 52 (2023) 239–251.
[8] H. Zhang, Y. Liu, L. Wang, Z. Li, X. Lu, T. Yang, J. Ma, Enhanced radical generation in an ultraviolet/chlorine system through the addition of TiO_2, Environ. Sci. Technol. 55 (2021) 11612–11623.
[9] G. Miao, M. Zhou, Y. Zhang, Z. Yang, Y. Liu, Nanoarchitectonic composites with direct z-scheme heterojunction of $CsPbBr_3$ quantum dot/$CuCo_2O_4$ nanosheet for efficient photocatalytic CO_2 reduction, J. Alloys. Compd. 925 (2022) 166733.
[10] J. Lin, J. Du, Y. Zhu, Z. Chen, M. Wang, J. Zeng, Z. Li, D. Li, D. Gao, D. Wang, Enhanced piezoelectric photocatalytic activity of MXene/ZnS/Fe_3O_4 via three-in-

one strategy based on dual Schottky heterojunction, interface electric field, and oxygen vacancy for pollutant degradation and removal, Water. Res. 273 (2024) 123040.
[11] Q. Wang, M. Yu, W. Xu, D. Li, X. Lin, Y. Liu, S. Zhu, J. Jia, Photo-generation of hole dominated selective degradation of hydrophobic organic pollutants with tetracyanoquinodimethane (TCNQ)-modified $BiOIO_3$ catalyst, Chem. Eng. J. 504 (2025) 159036.
[12] Y. Zhang, Z. Zhang, Y. Zhang, Y. Li, Y. Yuan, Shape-dependent synthesis and photocatalytic degradation by Cu_2O nanocrystals: kinetics and photocatalytic mechanism, J. Colloid. Interface Sci. 651 (2023) 117–127.
[13] S. Li, R. Yan, M. Cai, W. Jiang, M. Zhang, X. Li, Enhanced antibiotic degradation performance of $Cd_{0.5}Zn_{0.5}S/Bi_2MoO_6$ S-scheme photocatalyst by carbon dot modification, J. Mater. Sci. Technol. 164 (2023) 59–67.
[14] Y. Wei, L. Xu, Z. Yin, Y. Li, Q. Wang, J. Han, J. Qiu, Z. Yang, Z. Song, Atom-sharing Bi/Bi_3O_4Br plasmonic heterojunctions with effectively boosted photoelectrochemical activity for specific detection of chlorpyrifos, Colloids Surfaces A 683 (2024) 133053.
[15] D. Mao, J. Yuan, X. Qu, C. Sun, S. Yang, H. He, Size tunable Bi_3O_4Br hierarchical hollow spheres assembled with {0 0 1}-facets exposed nanosheets for robust photocatalysis against phenolic pollutants, J. Catal. 369 (2019) 209–221.
[16] Q. Wang, W. Wang, L. Zhong, D. Liu, X. Cao, F. Cui, Oxygen vacancy-rich 2D/2D $BiOCl\text{-}g\text{-}C_3N_4$ ultrathin heterostructure nanosheets for enhanced visible-light-driven photocatalytic activity in environmental remediation, Appl. Catal. B 220 (2018) 290–302.
[17] J. Di, J. Xia, M.F. Chisholm, J. Zhong, C. Chen, X. Cao, F. Dong, Z. Chi, H. Chen, Y. X. Weng, J. Xiong, S.Z. Yang, H. Li, Z. Liu, S. Dai, Defect-tailoring mediated electron–Hole separation in single-unit-cell Bi_3O_4Br nanosheets for boosting photocatalytic hydrogen evolution and nitrogen fixation, Adv. Mater. 31 (2019) e1807576.
[18] J. Di, Y.L. Liu, Y. Zhang, S.S. Guo, S.W. Wang, W. Jiang, H.M. Li, J.X. Xia, In situ N-doped $Bi_3O_4Br/(BiO)_2CO_3$ ultrathin nanojunctions with matched energy band structure for nonselective photocatalysis pollutant removal, cMat 1 (2024) 3006. -2691.
[19] Q. Wang, G. Lv, Y. Cao, Z. Chen, J. Jia, Y. Qin, Z. Lin, X. Xie, Z. Wang, Rational design of 2D ultrathin $BiO(HCOO)_xI_{1-x}$ composite nanosheets: the synergistic effect of ultrathin structure and hybridization in the effective elimination of BPA under visible light irradiation, Sep. Purif. Technol. 282 (2022) 120153.
[20] H. Hu, J. Jin, M. Xu, C. Xu, Y. Cheng, W. Ji, Z. Ding, M. Shao, Y. Wan, Novel Z-scheme Bi_3O_4Br/NH_2-MIL-125(Ti) composite for efficient photocatalytic degradation of tetracycline, Opt. Mater. 135 (2023) 113262.
[21] M. Fu, M. Yang, J. Bai, Y. Li, M. Fang, P. Lu, X. Kuang, Analysis of novel In_2S_3/polyimide Z-scheme heterojunctions with enhanced photocatalytic target compound degradation efficiency, J. Environ. Chem. Eng. 12 (2024) 112029.
[22] X. Shi, W. Dai, Y. Bai, G. Luo, X. Dong, Q. Ren, L. Ye, Modulating internal electric field by oxygen vacancy engineering and consequent forming quantum wells for boosted selective CO_2 photoreduction, Appl. Catal. B 343 (2024) 123523.
[23] J. Zeng, X. Wang, B. Xie, Q. Li, X. Zhang, Large π-conjugated metal-organic frameworks for infrared-light-driven CO_2 reduction, J. Am. Chem. Soc. 144 (2022) 1218–1231.
[24] C. Qiu, H. Zhang, Q. Li, Y. Guo, Y. Song, F. An, L. Zhu, A. Xiao, C. Lv, D. Zhang, $PANI/CoMoO_4$ nanocomposite heterostructures for detection of NH_3 at room temperature, ACS. Appl. Nano Mater. 7 (2023) 857–865.
[25] O.S. Ekande, M. Kumar, Review on polyaniline as reductive photocatalyst for the construction of the visible light active heterojunction for the generation of reactive oxygen species, J. Environ. Chem. Eng. 9 (2021) 105725.
[26] L. Liu, L. Ding, Y. Liu, W. An, S. Lin, Y. Liang, W. Cui, A stable Ag_3PO_4@PANI core@shell hybrid: enrichment photocatalytic degradation with π-π conjugation, Appl. Catal. B 201 (2017) 92–104.
[27] X. Liu, L. Cai, A novel double Z-scheme BiOBr-GO-polyaniline photocatalyst: study on the excellent photocatalytic performance and photocatalytic mechanism, Appl. Surf. Sci. 483 (2019) 875–887.
[28] Y. Qing, Y. Li, L. Cao, Y. Yang, L. Han, P. Dansawad, H. Gao, W. Li, Rationally designed C-PANI/BiOBr STEP-scheme heterojunction photocatalyst for boosting photodegradation of 17β-estradiol, Sep. Purif. Technol. 314 (2023) 123545.
[29] S. Sk, I. Mondal, A. Mahata, B.M. Abraham, C. Nayak, D. Bhattacharyya, S.N. Jha, R. Ghosh, U. Pal, Function of defects in NH_2-MIL-125@PANI@Co_3O_4 photocatalyst for efficient hydrogen evolution, ACS. Appl. Energy Mater. 5 (2022) 12324–12335.
[30] J. Hu, F. Chen, K. Mu, J. Zhang, J. Lu, Enhanced photocatalytic O_2 activation by the synergy of efficient oxygen adsorption and interfacial charge separation: a case of Bi_3O_4Br/rGO van der Waals heterojunction, Sep. Purif. Technol. 286 (2022) 120416.
[31] J. Di, J. Xia, M.F. Chisholm, J. Zhong, C. Chen, X. Cao, F. Dong, Z. Chi, H. Chen, Y. X. Weng, J. Xiong, S.Z. Yang, H. Li, Z. Liu, S. Dai, Defect-tailoring mediated electron-hole separation in single-unit-cell Bi(3) O(4) Br nanosheets for boosting photocatalytic hydrogen evolution and nitrogen fixation, Adv. Mater. 31 (2019) e1807576.
[32] F. Wang, T. Lu, X. Cheng, Y. Zhang, X. Xiao, Fabrication of $MoSe_2/Bi_3O_4Br$ Z-scheme heterojunction with enhanced photocatalytic performance, J. Environ. Chem. Eng. 12 (2024) 111991.
[33] H. Wu, D. Wang, P. Zhou, M. Xie, J. Jing, Y. Xu, J. Xie, Probing effective charge migration and highly improved photocatalytic activity on polyaniline/$Zn_3In_2S_6$ nano-flower under long wavelength light, Sep. Purif. Technol. 274 (2021) 119004.
[34] J. Di, C. Chen, S.-Z. Yang, S. Chen, M. Duan, J. Xiong, C. Zhu, R. Long, W. Hao, Z. Chi, H. Chen, Y.-X. Weng, J. Xia, L. Song, S. Li, H. Li, Z. Liu, Isolated single atom cobalt in Bi_3O_4Br atomic layers to trigger efficient CO_2 photoreduction, Nat. Commun. 10 (2019) 2840.
[35] C. Wang, K. Rong, Y. Liu, F. Yang, S. Li, Carbon quantum dots-modified tetra (4-carboxyphenyl) porphyrin/BiOBr S-scheme heterojunction for efficient photocatalytic antibiotic degradation, Sci. China Mater. 67 (2024) 562–572.
[36] S. Li, C. Wang, K. Dong, P. Zhang, X. Chen, X. Li, MIL-101(Fe)/BiOBr S-scheme photocatalyst for promoting photocatalytic abatement of Cr(VI) and enrofloxacin antibiotic: performance and mechanism, Chin. J. Catal. 51 (2023) 101–112.
[37] J. Di, J. Xia, M. Ji, B. Wang, S. Yin, Q. Zhang, Z. Chen, H. Li, Advanced photocatalytic performance of graphene-like BN modified BiOBr flower-like materials for the removal of pollutants and mechanism insight, Appl. Catal. B 183 (2016) 254–262.
[38] R. Li, H. Chen, J. Xiong, X. Xu, J. Cheng, X. Liu, G. Liu, A mini review on bismuth-based Z-scheme photocatalysts, Materials. (Basel) 13 (2020) 13225057.
[39] Y.M. Huang, Y. Yu, Y.F. Yu, B. Zhang, Oxygen vacancy engineering in photocatalysis, Sol. RRL. 4 (2020) 2000037.
[40] C. Li, T. Sun, G. Yi, D. Zhang, Y. Zhang, X. Lin, J. Liu, Z. Shi, Q. Lin, Fabrication of a $Ag/CNQDs/g\text{-}C_3N_4$-PVDF photocatalytic composite membrane with excellent photocatalytic and self-cleaning properties, J. Environ. Chem. Eng. 10 (2022) 108488.
[41] K. Gao, L.-a. Hou, X. An, D. Huang, Y. Yang, $BiOBr/MXene/gC_3N_4$ Z-scheme heterostructure photocatalysts mediated by oxygen vacancies and MXene quantum dots for tetracycline degradation: process, mechanism and toxicity analysis, Appl. Catal. B 323 (2023) 122150.
[42] W. Tang, G. Zeng, J. Gong, J. Liang, P. Xu, C. Zhang, B.-B. Huang, Impact of humic/fulvic acid on the removal of heavy metals from aqueous solutions using nanomaterials: a review, Sci. Total Environ. 468-469 (2014) 1014–1027.
[43] J. Yu, Z. Gong, S. Wang, H. Zhong, Y. Tao, Y. Hou, Q. Fu, H. Yang, J. Li, J. Wang, Z. Hao, G. Ouyang, Two major deactivation mechanisms in carbon-based advanced oxidation processes (AOPs) dominated by electron-transfer pathway (ETP), Appl. Catal. B (2025) 364.
[44] S. Wang, Z. Shang, J. Xu, L. Xiong, C. Yu, F. Geng, H. Wu, X. Yang, Y. Yang, J. Lv, L. Zhao, Y. Wang, G. Jiang, Unexpected persistent production of H2O2 during tetrabromobisphenol A photocatalytic degradation based on interface carrier regulation, Appl. Catal. B (2025) 371.
[45] D. Ke, B. Sun, Y. Zhang, F. Tian, Y. Chen, Q. Meng, Y. Zhang, Z. Hu, H. Yang, C. Yang, X. Xiong, T. Zhou, Designing atomic Ni/Cu pairs on a reactive BiOCl surface for efficient photo-chemical HCO_3^--to-CO conversion, J. Mater. Chem. A 12 (2024) 19950–19957.
[46] J. Liu, N. Ma, W. Wu, Q. He, Recent progress on photocatalytic heterostructures with full solar spectral responses, Chem. Eng. J. 393 (2020) 124719.
[47] G.Q. Huang, W.N. Ye, C.X. Lv, D.S. Butenko, C. Yang, G.L. Zhang, P. Lu, Y. Xu, S. C. Zhang, H.W. Wang, Y.K. Zhu, D.J. Yang, Hierarchical red phosphorus incorporated TiO hollow sphere heterojunctions toward superior photocatalytic hydrogen production, J. Mater. Sci. Technol. 108 (2022) 18–25.
[48] Z. Wang, W. Xu, X. Chen, Y. Peng, Y. Song, C. Lv, H. Liu, J. Sun, D. Yuan, X. Li, X. Guo, D. Yang, L. Zhang, Defect-rich nitrogen doped Co_3O_4/C porous nanocubes enable high-efficiency bifunctional oxygen electrocatalysis, Adv. Funct. Mater. 29 (2019) 1902875.
[49] B. Liu, B. Zhang, J. Ji, K. Li, J. Cao, Q. Feng, H. Huang, Effective regulation of surface bridging hydroxyls on TiO_2 for superior photocatalytic activity via ozone treatment, Appl. Catal. B 304 (2022) 120952.
[50] S. Li, K. Dong, M. Cai, X. Li, X. Chen, A plasmonic S-scheme Au/MIL-101(Fe)/BiOBr photocatalyst for efficient synchronous decontamination of Cr(VI) and norfloxacin antibiotic, eScience 4 (2024).
[51] W. Cai, X. Yu, Y. Cao, C. Hu, Y. Wang, Y. Zhao, Y. Bu, Electron-coupled enhanced interfacial interaction of Ce-MOF/Bi_2MoO_6 heterostructure for boosted photoreduction CO_2, J. Environ. Chem. Eng. 10 (2022) 107461.
[52] J.J. Yu, X. Wang, L. Chen, G.H. Lu, G.S. Shi, X.F. Xie, Y. Wang, J. Sun, Enhanced adsorption and visible-light photocatalytic degradation of toluene by CQDs/UiO-66 MOG with hierarchical pores, Chem. Eng. J. 435 (2022) 135033.
[53] Z. Zhang, S. Lin, X. Li, H. Li, T. Zhang, W. Cui, Enhanced photocatalytic activity toward organic pollutants degradation and mechanism insight of novel CQDs/$Bi_2O_2CO_3$ composite, Nanomaterials (Basel) 8 (2018) 8050330.
[54] X. Zhang, B. Lin, X. Li, X. Wang, K. Huang, Z. Chen, MOF-derived magnetically recoverable Z-scheme $ZnFe_2O_4/Fe_2O_3$ perforated nanotube for efficient photocatalytic ciprofloxacin removal, Chem. Eng. J. 430 (2022) 132728.
[55] T. Han, X. Cao, H.C. Chen, J. Ma, Y. Yu, Y. Li, W. Xu, K. Sun, A. Huang, Z. Chen, C. Chen, H. Zhang, B. Ye, Q. Peng, Y. Li, Photosynthesis of benzonitriles on BiOBr nanosheets promoted by vacancy associates, Angew. Chem. Int. Ed. Engl. 62 (2023) e202313325.
[56] X. Yi, H. Ji, C. Wang, Y. Li, Y. Li, C. Zhao, A. Wang, H. Fu, P. Wang, X. Zhao, W. Liu, Photocatalysis-activated SR-AOP over PDINH/MIL-88A(Fe) composites for boosted chloroquine phosphate degradation: performance, mechanism, pathway and DFT calculations, Appl. Catal. B-Environ. 293 (2021) 120229.
[57] X. Peng, J. Wu, Z. Zhao, X. Wang, H. Dai, Y. Wei, G. Xu, F. Hu, Activation of peroxymonosulfate by single atom Co-N-C catalysts for high-efficient removal of chloroquine phosphate via non-radical pathways: electron-transfer mechanism, Chem. Eng. J. 429 (2022) 132245.